Van der Waals Heterostructure Polaritons with Moiré-Induced Nonlinearity

Long Zhang[1,2], Fengcheng Wu[3], Shaocong Hou[4], Zhe Zhang[1], Yu-Hsun Chou[5], Kenji Watanabe[6], Takashi Taniguchi[7], Stephen R. Forrest[1,4] and Hui Deng[1*]

[1] *Physics Department, University of Michigan, 450 Church Street, Ann Arbor, MI 48109-2122, USA*

[2] *Department of Physics, Xiamen University, Xiamen 361005, Fujian, China*

[3] *Condensed Matter Theory Center and Joint Quantum Institute, Department of Physics, University of Maryland, College Park, Maryland 20742, USA*

[4] *Department of Electrical Engineering and Computer Science, University of Michigan, 450 Church Street, Ann Arbor, MI 48109-1040, USA*

[5] *Department of Photonics, National Cheng Kung University, No. 1, University Road, East District, Tainan City 70101, Taiwan, ROC*

[6] *Research Center for Functional Materials, National Institute for Materials Science, Tsukuba, Japan and*

[7] *International Center for Materials Nanoarchitectonics, National Institute for Materials Science, Tsukuba, Japan*

[*] dengh@umich.edu

Controlling matter-light interactions with cavities is of fundamental importance in modern science and technology [1]. It is exemplified in the strong-coupling regime, where matter-light hybrid modes form, with properties controllable via the photon component on the optical-wavelength scale [2, 3]. In contrast, matter excitations on the nanometer scale are harder to access. In two-dimensional van der Waals heterostructures, a tunable moiré lattice potential for electronic excitations may form [4], enabling correlated electron gases in lattice potentials [5–9]. Excitons confined in moiré lattices [10, 11] have also been reported, but cooperative effects have been elusive and interactions with light have remained perturbative [12–15]. Here, integrating $MoSe_2$ -WS_2 heterobilayers in a microcavity, we establish cooperative coupling between moiré -lattice excitons and microcavity photons up to liquid-nitrogen temperature, thereby integrating into one platform versatile control over both matter and light. The density dependence of the moiré polaritons reveals strong nonlinearity due to exciton blockade, suppressed exciton energy shift, and suppressed excitation-induced dephasing, all of which are consistent with the quantum-confined nature of the moiré excitons. Such a moiré polariton system combines strong nonlinearity and microscopic-scale tuning of matter excitations with the power of cavity engineering and long range coherence of light, providing a new platform for collective phenomena from tunable arrays of quantum emitters.

I. INTRODUCTION

Controlling matter-light interactions has mostly been implemented with either microscopic, individual quantum particles, or macroscopic ensembles of free particles that often can be modelled classically. Bridging the two limits to realize collective coupling among arrays of quantum particles ushers new paradigms in quantum many-body physics and quantum simulation research, such as been pursued using atomic optical lattices and cavities [16–18]. In solid state systems, however, such a pursuit has been exceedingly difficult, for nonlinearity is often too weak, due to screened Coulomb interactions, and inhomogeneity, too large. In this work, we show that moiré lattices formed in hetero-bilayer (hBL) transition metal dichalcogenides (TMDCs) crystals may provide a platform that overcomes these limitations of conventional solids.

When two monolayer (ML) crystals are placed together, a moiré lattice can form due to a slight mismatch in the lattice constants or crystal orientations of the MLs [4, 10, 11]. Its period is tunable by the twist angle between the ML crystals from a few to a few tens of nanometers –

comparable to the range of Coulomb interactions in semiconductors. The natural formation of the moiré lattice promises the prospect of uniformity among different moiré cells across the lattice, thereby potentially enabling a new solid-state platform for cooperative phenomena between light and arrays of nonlinear quantum particles. While exciton states induced by the moiré lattice have been reported [12–15], the fundamental question remains whether a sufficiently uniform lattice of quantized excitations can be formed in a moiré system. Exciton-light interactions have remained in the perturbative regime, and cooperative phenomena have not been reported.

II. MOIRÉ POLARITONS IN WS_2 -$MOSE_2$ HETERO-BILAYERS

To enable cooperative coupling between moiré excitons and photons, we use WS_2 -$MoSe_2$ hBLs enclosed in a microcavity (Fig. 1a). The hBL is encapsulated in hexagon boron nitride (hBN) with a twist angle measured to be $56.5^\circ \pm 0.9^\circ$ (Extended Data Fig.1). The WS_2 -$MoSe_2$ hBL is unique among commonly studied TMDCs hBLs in that the two lowest-energy moiré exciton modes have large oscillator strengths, inherited from that of the ML $MoSe_2$ A exciton.[15, 19, 20]. This not only allows ready identification of moiré excitons via the absorption spectra, but also suggests both of the moiré excitons may strongly couple with light and form stable moiré polaritons.

We first identify the existence of moiré lattice and moiré excitons before enclosing the hBL in a cavity. As shown by comparison of the hBL and ML reflection spectra in Fig. 1c, the ML $MoSe_2$ A exciton is split into two moiré excitons in the hBL, X_1 and X_2, separated by about 40 meV, both with pronounced absorption, consistent with calculations (Fig. 1b-c) and temperature dependence of the hBL (Extended Data Fig.2).

When the hBL is placed at the anti-node of a $\lambda/2$ microcavity (Fig. 1d, see Extended Data Fig.3 for more details of the cavity), in place of the moiré excitons or the bare cavity, three dispersive modes are observed up to 70 K, as shown in Fig. 2a-b. The modes anti-cross at the two moiré exciton resonances, showing clearly strong coupling of both moiré excitons (X_1 and X_2) with the cavity photon. Emission, temperature dependence, and time resolved studies are provided in the Extended Data Fig. 4-6.

The measured dispersions (Fig. 2d-e) are described very well by calculations based on a three

coupled oscillator model with a Hamiltonian:

$$H = \begin{bmatrix} E_{X_1} & 0 & \Omega_1 \\ 0 & E_{X_2} & \Omega_2 \\ \Omega_1 & \Omega_2 & E_c \end{bmatrix}.$$

Here E_c is the energy of the cavity mode, E_{X_1,X_2} are the energies of the two moiré excitons, and $\Omega_{1,2}$ are their coupling strengths with the cavity photon. The three distinct dispersions measured correspond to the three new, light-matter hybrid eigen-modes of the Hamiltonian: the upper (UP), middle (MP) and lower (LP) polaritons. The fitted E_{X_1,X_2} agree with the independently measured moiré excitons energies (Fig. 1c) within 5 meV, where the difference is commonly observed as a result of strain due to deposition of the top mirror. The fitted $\Omega_{1,2} = 10.1 \pm 0.3$ meV and 8.5 ± 0.3 meV at 4 K and change slightly to 9.6 ± 0.4 meV and 8.7 ± 0.4 meV at 70 K. From independent measurement, the exciton half linewidths increase from $\gamma_{X_1,X_2} = 7.5$ meV and 8.4 meV at 4 K to 8.8 meV and 8.9 meV at 70 K (Extended Data Fig.5), which are mainly due to inhomogeneous broadening [21]. The strong coupling condition $\Omega_{1,2} > (\gamma_c + \gamma_{X_{1,2}})/2$ is satisfied up to 70 K.

In comparison, a similar cavity enclosing a ML $MoSe_2$ also exhibits clearly strong coupling of the ML $MoSe_2$ A-exciton and the cavity photon (Fig. 2c and f). Fitting the dispersions of the polaritons yield Ω_{XA}=17.1±0.1 meV, which is comparable to but slightly larger than $\sqrt{\Omega_1^2 + \Omega_2^2}$=13.2 meV. This confirms that most of the oscillator strength of the ML $MoSe_2$ A-exciton is distributed to the moiré states X_1 and X_2. The reduction may be due to additional, higher-energy moiré states [7, 15] or additional disorder introduced into the bilayer during stacking of the MLs.

III. ZERO-DIMENSIONALITY OF MOIRÉ EXCITONS

With robust polariton modes formed with both moiré hBL and ML excitons, we study the effect of the underlying moiré lattice via their nonlinear response to the excitation density n. We focus on $n < n_{Mott} = 1/a_B^2 \sim 10^6$ μm^{-2}, for n_{Mott} the Mott density and $a_B \sim 1$ nm the Bohr radius [22], and vary n from 10 μm^{-2} up to 3×10^4 μm^{-2} using a resonant 150 fs pulsed laser (see Methods for details) [23–26]. A few representative reflectance spectra at different excitation densities are shown in Fig. 3a-b for the hBL- and ML-cavities, respectively. Fitting the absorption dips in the spectra with Lorentzian functions, we obtain the polariton energies as plotted in Fig. 3c-d.

With increasing excitation densities, the moiré LP and MP shift symmetrically toward the moiré exciton resonance E_{X_1} while their linewidths remain the same (Fig. 3a and Fig. 3c). These suggest reduced exciton-photon coupling strength, yet constant exciton energy or dephasing, which are typical properties of 0D excitons. In sharp contrast, the ML LP and UP shift together to higher energies, accompanied by significant linewidth broadening. These suggest a much weaker saturation of the exciton-photon coupling strength but pronounced many-body effects, as expected of 2D excitons.

To analyze the density dependence quantitatively, we use the coupled-oscillator model to extract from the polariton spectra the three basic properties of excitons: the exciton energy $E_X(n)$, linewidth $\gamma_X(n)$, and photon coupling strength $\Omega(n)$ (see Methods for details). The results can be compared with well-established models for free 2D excitons:

$$E_X(n) = E_X(0) + \beta_1 n - \beta_2 n^2, \tag{1}$$

$$\gamma_{X,n} = \gamma_X(0) + \alpha n, \tag{2}$$

$$\Omega(n) = \Omega(0)/\sqrt{1 + \frac{n}{n_s}}. \tag{3}$$

These equations describe the energy shift due to two and three-particle exchange interactions with coefficients $\beta_{1,2}$[24], the linewidth broadening due to exciton-induced dephasing (EID) with coefficient α [27], and oscillator strength saturation due to Pauli blocking with a saturation density n_s [22, 28].

Pronounced differences between moiré and ML-excitons are clearly seen in all three properties (Fig. 4a-c). For the ML exciton, all three properties are described very well by Eqs. 1-3 for 2D excitons (blue diamonds and lines in Fig. 4a-c). The exciton energy blueshifts by 1.5 meV due to exchange interactions, the linewidth broadens significantly by 3 meV due to EID. The fitted coefficients, $\beta_{1,ML} = (1.2 \pm 0.1) \times 10^{-1}$ μeV$\cdot\mu$m^2, $\beta_{2,ML} = (2.9 \pm 0.4) \times 10^{-6}$ μeV$\cdot\mu$m^4, and $\alpha = 0.11 \pm 0.01$ μeV$\cdot\mu$m^2, all agree well with reported values [24, 27]. The coupling strength decreases slightly by up to 5%; the corresponding $n_{s,ML} = (2.8 \pm 0.4) \times 10^5$ μm^{-2} is comparable to $1/a_B^2 \sim 10^6$ μm^{-2}. These results confirm that the ML excitons behave as 2D particles; they also provide a consistency check of our density calibration.

In contrast to the ML excitons, the moiré excitons show no measurable energy shift, a much smaller line-broadening of < 1 meV, and a much stronger saturation of the coupling strength by up to 20% (Fig. 4a-c, red circles). These can not be explained with the 2D exciton picture, but

are expected of 0D excitons, as we discuss below.

In a moiré lattice, the exciton center-of-mass wavefunction is no longer a plane wave, but becomes localized near the potential minimum of each moiré cell, with a localization length ℓ ($a_B < \ell < a_M/2$, where a_M is the moiré period), as illustrated in Fig. 4d. Evaluating ℓ for our device of $a_M = 4.2$ nm yields $\ell = 1.2$ nm. Therefore the confinement leads to an increase of the effective local density n_{eff} by $(a_M/2\ell)^2 \sim 3$ at the potential minima, and thus enhanced exchange and dipole-dipole interactions. If the moiré exciton are 2D-like band excitons, the enhanced interactions should lead to correspondingly an enhanced energy shift and enhanced EID. On the contrary, we observe no energy shift and a much smaller line-broadening. Therefore, our observations show the moiré excitons in our device are no longer 2D band excitons.

On the other hand, the suppressed energy shift and linewidth broadening are characteristic of quantum dots with strong exciton blockade. Exciton blockade takes place when the interaction energy between two excitons in the same cell becomes greater than the exciton linewidth, so that multiple excitations correspond to distinct, quantized energy levels. In our hBL, the on-site exchange interaction $U_{exc,hBL} = \frac{1}{2\pi}(\frac{a_B}{w})^2 E_b \sim 40$ meV for binding energy $E_b \sim 250$ meV, and exciton wavefunction extension $w \sim$1 nm. The dipole interaction due to the inter-layer component is $U_{dd,hBL} \sim \frac{d}{a_B} U_{exc,hBL} \sim 30$ meV for dipole length $d \sim$0.7 nm [11]. These values agree with a more detailed calculation (Extended Data Fig.9) and are much larger than the exciton full linewidth of $2\gamma_{X_1} \sim 15$ meV. So we indeed expect exciton blockade in a moiré cell. At the same time, since both the exchange and dipole-dipole interactions decrease quickly with distance, they are both suppressed for excitons in different moiré cells (Extended data Fig.9). The intra-cell exciton blockade, together with suppressed inter-cell interactions, lead to suppressed many-body effects for the single-exciton resonance, which manifests as absence of energy shift or EID, in agreement with our observations.

Consistent with exciton blockade, exciton-photon coupling saturates at one exciton per moiré cell, or, $n_s \sim 1/a_M^2 \sim (\pi a_B^2/a_M^2) n_{s,ML} \sim 6 \times 10^4$, in excellent agreement with the fitted $n_{s,hBL} = (6.5 \pm 0.3) \times 10^4$ μm^{-2} for $n \geq 1000$ μm^{-2} (bottom solid line in Fig. 4c). In contrast, if the moiré excitons are 2D band excitons, n_s would have remained the same as $n_{s,ML}$, since the total oscillator strength is conserved in the band across the lattice. We note that the fit does not explain the abnormally strong saturation at very low densities of $n < 1000$ μm^{-2}, which we will discuss more later.

IV. MOIRÉ LATTICE-INDUCED NONLINEARITY OF MOIRÉ POLARITONS

The distinctly different density dependence of the moiré polaritons shown above suggests the possibility of achieving a much higher polariton nonlinearity, even for polariton modes that are stable at high temperatures. Fig. 4e shows the measured $g(n) = \mid dE(n)/dn \mid$ for both the moiré and ML LPs (symbols).

While the nonlinearity increases with decreasing density for both moiré and ML LPs, the moiré LPs show surprisingly a larger nonlinearity. The nonlinearity of ML LPs originates primarily from exciton exchange-interactions and g_{ML-LP} saturates below $n \sim 1000$ μm^{-2} to 0.02 μeV$\cdot\mu$m^2 (0.04 μeV$\cdot\mu$m^2) at the measured (zero) detuning, in agreement with reported values [24, 26, 29]. The nonlinearity of moiré LPs results primarily from exciton blockade. Based on the data at $n > 1000$ μm^{-2}, we obtain g_{hBL-LP} about four times higher than g_{ML-LP}.

At very low densities of $n < 1000$ μm^{-2}, while the ML polaritons or excitons show no measurable shift, the moiré polaritons show clearly saturation-induced shifts down to $n \sim 10$ μm^{-2} (Fig. 3c), corresponding to a stronger exciton saturation than expected from exciton blockade, exciton-interactions, or effects of trions and defect states (Fig. 4c) [30]. However, this abnormally large nonlinearity is repeatable over multiple measurements in multiple devices (see Extended Data Fig.7 for another example), suggesting hidden mechanisms for large polariton nonlinearity in moiré lattices. Phenomenologically, $\Omega_{X1}(n)$ over the full density range can be described very well by Eq. 3 if n_s is replaced by a density-dependent effective saturation density $n_{eff,s} = \tilde{n}_s(1 - Ae^{-n/B})$, for fitted $\tilde{n}_s = (4.4 \pm 0.1) \times 10^4$ μm^{-2}, $A = 0.98 \pm 0.04$ and $B = (7.4 \pm 0.5)$ μm^{-2} (Fig. 4c).

The polariton nonlinearity is a key figure of merit that distinguishes polariton systems from pure photon systems. Together with the robust coherence enforced by the photon component, it gives rise to a wide range of novel nonlinear many-body and quantum phenomena [31–36].

For polaritons made of 2D excitons, however, larger g is obtained only at the compromise of Ω, or the stability of polariton modes. This is because the exciton-exchange interaction and the exciton-photon coupling strength saturation, the two main contributions to g, both decrease with the exciton reduced mass μ: $g_{exc} \sim E_b a_B^2 \propto 1/\mu$ and $g_{sat} \propto a_B^2 \propto 1/\mu^2$. Yet the exciton-photon coupling strength $\Omega \propto \sqrt{f} \propto 1/a_B \propto \mu$. The highest polariton nonlinearity is achieved in single or few quantum-well GaAs microcavities [34, 35], with $g \sim 3$ μeV$\cdot\mu$m^2 and Ω only $\sim$3 meV. Wide-bandgap semiconductors, organic crystals and ML TMDCs all feature greater Ω and high-

temperature polaritons, yet a much weaker polariton nonlinearity [23, 26, 37, 38]. Higher order excitations in TMDCs, such as trions with strong band-filling effect [24, 29] and 2s excitons with a larger Bohr radius [25], have shown enhanced nonlinearity, but again at the compromise of stability.

The moiré polariton system uniquely combines strong nonlinearity, due to quantum confinement of excitons within each moiré cell, and a large total photon coupling strength, due to collective coupling among the cells. It thereby provides a new route to achieve strong nonlinearities simultaneously with robust exciton-photon coupling.

V. CONCLUSION

In summary, we have demonstrated the first polariton system formed via collective coupling of a 2D lattice of 0D excitons with light in a microcavity. The system therefore introduces quantum-dot like nonlinearity into cooperatively coupled solid state system, opening a door to novel quantum many-body physics and polariton devices [16–18, 39]. Polariton blockade and a strongly-correlated polariton gases may become possible with reduced inhomogeneous broadening of moiré excitons, improved cavity quality factors, and a better understanding of the abnormal enhancement of the polariton nonlinearity at very low excitation densities. Electrical gating and electrical field tuning of the heterobilayer can be implemented to further control the nonlinearity and many-body phenomena in the moiré polariton system.

METHODS

Sample fabrication. The ML $MoSe_2$, WS_2 and few layer hBN flakes were obtained by mechanical exfoliation from bulk crystals. A polyethylene terephthalate (PET) stamp was used to pick up the top hBN, WS_2 ML, $MoSe_2$ ML, and the bottom hBN under microscope. The WS_2 and $MoSe_2$ monolayer MLs were rotationally aligned to about 0° in the heterobilayer.

The bottom half of the cavity consists of 16 pairs of SiO_2/TiO_2 DBR with a $\lambda/4$ SiO_2 layer. The heterostructure on the PET stamp was stamped onto the bottom half of the cavity and the PET was dissolved in dichloromethane for six hours at room temperature. Then 67 nm PMMA film was spin coated on the top of heterobilayer to form the second half of the $\lambda/2$ cavity. Then a silver film of 40 nm thick was deposited using electron beam evaporation as the top mirror of the

cavity.

Optical measurements. For low temperature measurements, the sample was kept in a 4 K cryostat (Montana Instrument). The excitation and collection were carried out with a home-built confocal microscope with an objective lens with a numerical aperture (NA) of 0.42. To characterize the dispersion of the polariton device, we performed angle-resolved reflection measurement using white light from a tungsten halogen lamp. The white light was focused on the sample with a beam size of 10 μm in diameter. To perform power dependent reflection measurements, we used a 150 fs-pulse laser as the light source with a repetition rate of 80 MHz and focused beam size on the sample of around 1.5 μm in diameter. For the hBL, the laser was centered between LP and MP to simultaneously measure both modes, while the intensity at UP is negligible (Extended Data Fig.8 for an example spectrum of the laser). For the ML, due to the larger energy separation of the LP and UP, they were measured separately with the laser centered at each, respectively. The signal was detected using a Princeton Instruments spectrometer with a cooled charge-coupled camera.

Theory of moiré excitons The Hamiltonian for the moiré excitons is

$$\mathcal{H} = \begin{pmatrix} E_G + \frac{\hbar^2 \boldsymbol{k}^2}{2M_{\mathrm{X}}} & w(1 + e^{-i\boldsymbol{b}_+ \cdot \boldsymbol{r}} + e^{-i\boldsymbol{b}_- \cdot \boldsymbol{r}}) \\ w(1 + e^{i\boldsymbol{b}_+ \cdot \boldsymbol{r}} + e^{i\boldsymbol{b}_- \cdot \boldsymbol{r}}) & E_G + \delta_0 + \frac{\hbar^2 (\boldsymbol{k} - \boldsymbol{\kappa})^2}{2M_{\mathrm{IX}}} \end{pmatrix} \tag{4}$$

where E_G is an energy constant, M_{X} and M_{IX} are respectively the effective masses for intralayer and interlayer excitons, $\boldsymbol{\kappa} = (0, 4\pi/(3a_M))$ accounts for the momentum mismatch between the two excitons, and δ_0 is an energy offset. The off-diagonal terms are derived from interlayer tunneling, and $\boldsymbol{b}_\pm = 4\pi/(\sqrt{3}a_M)(\pm 1/2, \sqrt{3}/2)$. The moiré period is $a_M = a_0/\sqrt{\delta^2 + \theta^2}$, where $a_0 = (a_{\mathrm{MoSe_2}} + a_{\mathrm{WS_2}})/2 = 3.26$ Åand $\delta = |a_{\mathrm{MoSe_2}} - a_{\mathrm{WS_2}}|/a_0 \approx 4\%$. We use the following parameter values, $E_G = 1.61$eV, $\delta_0 = -20$ meV,$w = 14$ meV, $M_{\mathrm{X}} = 0.82m_0$, $M_{\mathrm{IX}} = 0.71m_0$, where m_0 is the electron bare mass. The energy spectrum of the moiré excitons is obtained by diagonalizing the moiré Hamiltonian $\mathcal{H}$ using plane-wave expansion, and is shown in Fig. 1b. For the lowest-energy exciton X_1, its interlayer component is plotted in Fig. 4d, which shows spatial localization.

Polariton density calibration In this section, we will use the bilayer device data as an example; the same procedure applies to the monolayer device. To extract the polariton density: First, we fit the reflection spectra in Fig. 3 using :

$$R = 1 - Absor_{LP} - Absor_{MP}, \tag{5}$$

where $Absor_{LP}$ and $Absor_{MP}$ represent absorption by the lower polariton (LP) and middle polari-

ton (MP) in the bilayer, respectively, and they are described by Lorentzian functions:

$$Absor_{LP,MP}(E) = \frac{A_{LP,MP}}{(E - E_{LP,MP})^2 + \gamma_{LP,MP}^2}, \tag{6}$$

Resonance energy $E_{LP,MP}$, linewidth (HWHM) $\gamma_{LP,MP}$, and absorption amplitude $A_{LP,MP}$ are fitting parameters with uncertainties $\delta_{E_{LP,MP}}, \delta_{\gamma_{LP,MP}}$ and $\delta_{A_{LP,MP}}$ corresponding to 95% confidence intervals.

We use pulsed laser with pulse duration of 150 fs and repetition rate f of 80 MHz. We calculate the polariton density n injected per pulse. The average power of the laser is P. The laser profile can be fitted with Gaussian function:

$$G(E) = \frac{A_{laser}}{\gamma_{laser}\sqrt{\pi/2}} e^{-\frac{2(E-E_{laser})^2}{\gamma_{laser}^2}} \tag{7}$$

where A_{laser} is the area of the Gaussian function, and γ_{laser} is the linewidth. The power absorbed by LP and MP, $P_{LP,MP}$ can be calculated using the convolution:

$$P_{LP,MP} = \frac{P \int G(E) Absor_{LP,MP}}{A_{laser}} = \frac{P \int G(E) \frac{A_{LP,MP}}{4(E-E_{LP,MP})^2 + \gamma_{LP,MP}^2}}{A_{laser}} \tag{8}$$

The total carrier density including both LP and MP created per pulse and its error δ_n can be calculated by:

$$n = (n_{LP} + n_{MP})/A_{beam} = (\frac{P_{LP}}{fE_{LP}} + \frac{P_{MP}}{fE_{MP}})/A_{beam}. \tag{9}$$

$$\delta_n = \sqrt{\delta_{n_{LP}}^2 + \delta_{n_{MP}}^2}/A_{beam} \tag{10}$$

Where, A_{beam}=1.5 μm, is the beam area, and $\delta_{n_{LP,MP}} = n_{LP,MP}\sqrt{(\frac{\delta_{P_{LP,MP}}}{P_{LP,MP}})^2 + (\frac{\delta_{E_{LP,MP}}}{E_{LP,MP}})^2}$

Extraction of exciton energy, linewidth, and coupling strength at different densities

To analyze the results quantitatively, we extract the density dependence of the exciton properties from the measured polariton spectra. In the heterobilayer cavity, we focus on the MP and LP modes and neglect changes caused by the X_2, since X_2 is at a much higher energy, and its change only negligibly affects MP and LP (see Extended Fig.10 for details). The cavity resonance energy E_c and linewidth γ_c are assumed to change negligibly with exciton density. Using the two coupled oscillator mode, the energies of the MP and LP of the heterobilayer cavity, as well as of the UP and LP of the ML-cavity can be extracted. In the following, we will use the bilayer device data as an example; the same procedure applies to the monolayer device.

$$\begin{aligned} E_{\mathrm{LP,MP}}(n) =& \frac{1}{2}\Big[E_X(n) + E_C + i(\gamma_C + \gamma_X(n))\Big] \\ & \pm\sqrt{\Omega(n)^2 + \frac{1}{4}\Big[E_X(n) - E_C + i(\gamma_C - \gamma_X(n))\Big]^2} \end{aligned} \tag{11}$$

Here the cavity resonance, E_C, and cavity half-linewidth γ_C, do not change with carrier density. Therefore, from the measured polariton energies and half-linewidth, $\gamma_{LP,MP}$, we obtain the density dependence of exciton energy, E_X, half-linewidth, γ_X, and exciton-photon coupling strength, Ω:

Exciton energy E_X and its uncertainty δ_{E_X} :

$$E_X(n) = E_{LP}(n) + E_{MP}(n) - E_C \tag{12}$$

$$\delta_{E_X} = \sqrt{\delta_{E_{LP}}^2 + \delta_{E_{MP}}^2 + \delta_{E_C}^2} \tag{13}$$

where, E_C and δ_{E_C} are the cavity resonance and its uncertainty obtained by fitting the angle resolved reflection spectrum in Fig. 3, and they do not change with polariton densities.

Exciton linewidth γ_X and its uncertainty δ_{γ_X}:

$$\gamma_X(n) = \gamma_{LP}(n) + \gamma_{MP}(n) - \gamma_C \tag{14}$$

$$\delta_{\gamma_X} = \sqrt{\delta_{\gamma_{LP}}^2 + \delta_{\gamma_{MP}}^2 + \delta_{\gamma_C}^2} \tag{15}$$

where, γ_C and δ_{γ_C} are the cavity linewidth and uncertainty obtained by fitting the reflection spectrum of the bare cavity in Fig. 1d, and they do not change with polariton densities.

Coupling strength Ω:

$$\Omega(n) = \frac{1}{2}\sqrt{\left[E_{LP}(n) - E_{MP}(n) + i(\gamma_{LP}(n) - \gamma_{MP}(n))\right]^2 - \left[E_X(n) - E_C + i(\gamma_X(n) - \gamma_C)\right]^2} \tag{16}$$

Dipole-dipole interaction The interlayer component of moiré excitons contributes to dipole-dipole interactions. The wave function for interlayer component of a moiré exciton localized near the potential minimum around the origin can be described as

$$W(\boldsymbol{r}_1, \boldsymbol{r}_2) = x_{\mathrm{IX}} \Phi(\frac{\boldsymbol{r}_1 + \boldsymbol{r}_2}{2}) \phi(\boldsymbol{r}_1 - \boldsymbol{r}_2), \tag{17}$$

where x_{IX} is the interlayer component weight, Φ and ϕ are respectively the center-of-mass and relative-mass wave function. We approximate Φ by a Gaussian $\Phi(\boldsymbol{R}) = \frac{1}{\sqrt{\pi}\ell} e^{-R^2/(2\ell^2)}$, and $\phi(\boldsymbol{r}) = \sqrt{8/\pi}(1/a_B)e^{-2r/a_B}$, where $\boldsymbol{R} = \frac{\boldsymbol{r}_1 + \boldsymbol{r}_2}{2}$, $\boldsymbol{r} = \boldsymbol{r}_1 - \boldsymbol{r}_2$, ℓ is the localization length that can be estimated using the exciton state shown in Fig. 4d, and a_B is the Bohr radius.

The dipole-dipole interaction between two excitons localized at different moiré sites can be approximated as

$$\begin{aligned} U_{dd}(\boldsymbol{L}) = & \int d\boldsymbol{r}_1 \int d\boldsymbol{r}_2 \int d\boldsymbol{r}_3 \int d\boldsymbol{r}_4 |W(\boldsymbol{r}_1, \boldsymbol{r}_2)|^2 |W(\boldsymbol{r}_3 - \boldsymbol{L}, \boldsymbol{r}_4 - \boldsymbol{L})|^2 \\ & [V_S(\boldsymbol{r}_1 - \boldsymbol{r}_3) + V_S(\boldsymbol{r}_2 - \boldsymbol{r}_4) - V_D(\boldsymbol{r}_1 - \boldsymbol{r}_4) - V_D(\boldsymbol{r}_2 - \boldsymbol{r}_3)] \\ = & 2x_{\mathrm{IX}}^2 \int \frac{d^2\boldsymbol{q}}{(2\pi)^2} V(\boldsymbol{q}) \frac{\exp(-q^2\ell^2/2)}{[1 + \frac{1}{64}a_B^{*2}q^2]^3} e^{-i\boldsymbol{q}\cdot\boldsymbol{L}}, \end{aligned} \tag{18}$$

where $\boldsymbol{L}$ is a moiré lattice vector, $V_S(\boldsymbol{r}) = e^2/(\epsilon r)$ is the intralayer Coulomb interaction, $V_D(\boldsymbol{r}) = e^2/(\epsilon\sqrt{r^2+d^2})$ is the interlayer Coulomb interaction with d the interlayer distance, and $V(\boldsymbol{q}) = \frac{2\pi e^2}{\epsilon q}(1-e^{-qd})$. To calculate $U_{dd}(\boldsymbol{L})$, we take $x_{\mathrm{IX}} \approx 1/\sqrt{2}$, $d = 0.65$ nm, $\epsilon = 5$, and $a_B \approx 1$ nm. Extended Fig.9 shows the onsite and nearest-neighbor dipole-dipole interactions as a function of twist angle. The onsite repulsion is sizable (~ 24 meV for a twist angle of 56.5°), while the offsite repulsion is negligible.

Data availability Data are available on request from the authors.

Competing interests The authors declare that they have no competing financial interests.

Author Contributions H.D., L.Z.conceived the experiment. L.Z. performed the measurements. F. W. provided theoretical inputs. L.Z. and Z.Z fabricated the device. L.Z. and H.D. performed data analysis. S.H deposited the silver mirror. Y.C grew the bottom DBR mirror. K.W. and T.T grew hBN single crystals. H.D. and S.F. supervised the projects. L.Z and H.D. wrote the paper with inputs from other authors. All authors discussed the results, data analysis and the paper.

Acknowledgment We are grateful for helpful discussions with Duncan Steel and Mack Kira. L. Z., S. H, S. F.and H. D.acknowledge the support by the Army Research Office under Awards W911NF-17-1-0312. L.Z. and H.D. also acknowledge the support by the Air Force Office of Scientific Research under Awards FA2386-18-1-4086 and by the National Science Foundation under Awards DMR-1838412. S. F. also acknowledges support from the U.S. Department of Energy, Office of Science, Office of Basic Energy Sciences, under Awards DE-SC0017971. F. W. is supported by the Laboratory for Physical Sciences. Y. C. acknowledge the support by the Young Scholar Fellowship Program by the Ministry of Science and Technology (MOST) in Taiwan, under Grant MOST 108-2636-M-006 -010. K. W. and T. T. acknowledge support from the Elemental Strategy Initiative conducted by the MEXT, Japan ,Grant Number JPMXP0112101001, JSPS KAKENHI Grant Numbers JP20H00354 and the CREST(JPMJCR15F3), JST.

REFERENCES

[1] Walther, H., Varcoe, B. T. H., Englert, B.-G. & Becker, T. Cavity quantum electrodynamics. *Reports on Progress in Physics* **69**, 1325–1382 (2006).

[2] Deng, H., Haug, H. & Yamamoto, Y. Exciton-polariton Bose-Einstein condensation. *Reviews of Modern Physics* **82**, 1489 (2010).

[3] Schneider, C. *et al.* Exciton-polariton trapping and potential landscape engineering. *Reports on Progress in Physics* **80**, 016503 (2016).

[4] Bistritzer, R. & MacDonald, A. H. Moiré bands in twisted double-layer graphene. *Proceedings of the National Academy of Sciences* **108**, 12233–12237 (2011).

[5] Dean, C. R. *et al.* Hofstadter's butterfly and the fractal quantum Hall effect in moiré superlattices. *Nature* **497**, 598–602 (2013).

[6] Cao, Y. *et al.* Unconventional superconductivity in magic-angle graphene superlattices. *Nature* **556**, 43–50 (2018).

[7] Tang, Y. *et al.* Simulation of Hubbard model physics in WSe_2/WS_2 moiré superlattices. *Nature* **579**, 353–358 (2020).

[8] Regan, E. C. *et al.* Mott and generalized Wigner crystal states in WSe_2/WS_2 moiré superlattices. *Nature* **579**, 359–363 (2020).

[9] Shimazaki, Y. *et al.* Strongly correlated electrons and hybrid excitons in a moiré heterostructure. *Nature* **580**, 472–477 (2020).

[10] Wu, F., Lovorn, T. & MacDonald, A. H. Topological exciton bands in moiré heterojunctions. *Physical Review Letters* **118**, 147401 (2017).

[11] Yu, H., Liu, G.-B., Tang, J., Xu, X. & Yao, W. Moiré excitons: From programmable quantum emitter arrays to spin-orbit–coupled artificial lattices. *Science Advances* **3**, e1701696 (2017).

[12] Jin, C. *et al.* Observation of moiré excitons in WSe_2/WS_2 heterostructure superlattices. *Nature* **567**, 76–80 (2019).

[13] Tran, K. *et al.* Evidence for moiré excitons in van der Waals heterostructures. *Nature* **567**, 71–75 (2019).

[14] Seyler, K. L. *et al.* Signatures of moiré-trapped valley excitons in $MoSe_2/WSe_2$ heterobilayers. *Nature* **567**, 66–70 (2019).

[15] Alexeev, E. M. *et al.* Resonantly hybridized excitons in moiré superlattices in van der Waals heterostructures. *Nature* **567**, 81–86 (2019).

[16] Ritsch, H., Domokos, P., Brennecke, F. & Esslinger, T. Cold atoms in cavity-generated dynamical optical potentials. *Reviews of Modern Physics* **85**, 553–601 (2013).

[17] González-Tudela, A., Hung, C.-L., Chang, D. E., Cirac, J. I. & Kimble, H. J. Subwavelength

vacuum lattices and atom–atom interactions in two-dimensional photonic crystals. *Nature Photonics* **9**, 320–325 (2015).

[18] Léonard, J., Morales, A., Zupancic, P., Esslinger, T. & Donner, T. Supersolid formation in a quantum gas breaking a continuous translational symmetry. *Nature* **543**, 87–90 (2017).

[19] Zhang, L. *et al.* Twist-angle dependence of moiré excitons in WS_2 /$MoSe_2$ heterobilayers. *Nature Communications* **11**, 5888 (2020).

[20] Tang, Y. *et al.* Tuning layer-hybridized moiré excitons by the quantum-confined Stark effect. *Nature Nanotechnology* 1–6 (2020).

[21] The oscillator strengths of the moiré and ML excitons correspond to radiative linewidths of 100s μeV and radiative decay rates of 100s fs. Therefore the measured linewidth of both types of excitons are still dominated by inhomogeneous broadening. The measured photoluminescence decay times are a few picoseconds for both moiré and ML excitons (Extended Data Fig.6), which are consistent with the expected very short radiative lifetime and are lengthened due to energy relaxation dynamics. The moiré excitons have broader linewidths (half width of $7-8$ meV) than the ML excitons (about 2 meV), likely due to inhomogeneity in lattice alignment or strain distribution introduced during transfer and stacking of the two MLs.

[22] Chernikov, A., Ruppert, C., Hill, H. M., Rigosi, A. F. & Heinz, T. F. Population inversion and giant bandgap renormalization in atomically thin WS_2 layers. *Nature Photonics* **9**, 466–470 (2015).

[23] Scuri, G. *et al.* Large Excitonic Reflectivity of Monolayer $MoSe_2$ Encapsulated in Hexagonal Boron Nitride. *Phys. Rev. Lett.* **120**, 037402 (2018).

[24] Emmanuele, R. P. A. *et al.* Highly nonlinear trion-polaritons in a monolayer semiconductor. *Nature Communications* **11**, 3589 (2020).

[25] Gu, J. *et al.* Enhanced nonlinear interaction of polaritons via excitonic rydberg states in monolayer WSe_2. *arXiv:1912.12544* (2019).

[26] Kravtsov, V. *et al.* Nonlinear polaritons in a monolayer semiconductor coupled to optical bound states in the continuum. *Light: Science & Applications* **9**, 56 (2020).

[27] Moody, G. *et al.* Intrinsic homogeneous linewidth and broadening mechanisms of excitons in monolayer transition metal dichalcogenides. *Nature Communications* **6**, 8315 (2015).

[28] Huang, D., Chyi, J.-I. & Morkoç, H. Carrier effects on the excitonic absorption in GaAs quantum-well structures: Phase-space filling. *Phys. Rev. B* **42**, 5147–5153 (1990).

[29] Tan, L. B. *et al.* Interacting Polaron-Polaritons. *Physical Review X* **10**, 021011 (2020).

[30] The strong saturation observed at very low excitation densities cannot be explained by trions or states in deeper trapping potentials. These states would have a small initial oscillator strength and lower resonance energy, so the increase of saturation density would have been accompanied by an increase of the coupling strength and exciton energy, in contradiction with our observations.

[31] Ballarini, D. *et al.* All-optical polariton transistor. *Nature Communications* **4**, 1778 (2013).

[32] Walker, P. M. *et al.* Ultra-low-power hybrid light matter solitons. *Nature Communications* **6**, 8317 (2015).

[33] Berloff, N. G. *et al.* Realizing the classical XY Hamiltonian in polariton simulators. *Nature Materials* **16**, 1120–1126 (2017).

[34] Delteil, A. *et al.* Towards polariton blockade of confined exciton–polaritons. *Nature Materials* **18**, 219–222 (2019).

[35] Muñoz-Matutano, G. *et al.* Emergence of quantum correlations from interacting fibre-cavity polaritons. *Nature Materials* **18**, 213–218 (2019).

[36] Kim, S. *et al.* Emergence of microfrequency comb via limit cycles in dissipatively coupled condensates. *Physical Review B* **101**, 085302 (2020).

[37] Daskalakis, K. S., Maier, S. A., Murray, R. & Kéna-Cohen, S. Nonlinear interactions in an organic polariton condensate. *Nature Materials* **13**, 271–278 (2014).

[38] Barachati, F. *et al.* Interacting polariton fluids in a monolayer of tungsten disulfide. *Nature Nanotechnology* **13**, 906–909 (2018).

[39] Yu, H. & Yao, W. Electrically tunable topological transport of moiré polaritons. *Science Bulletin* **65**, 1555–1562 (2020).

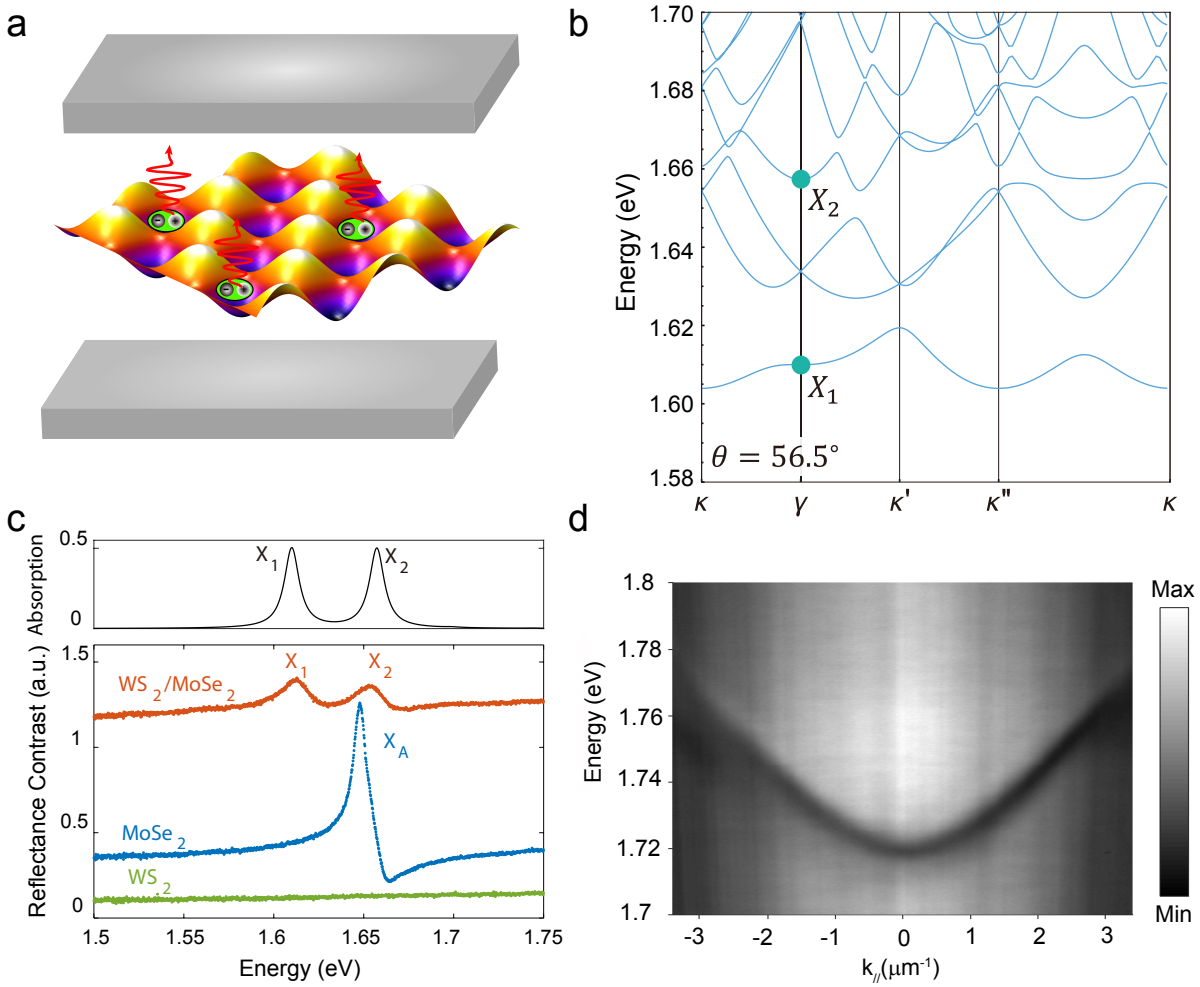

FIG. 1: **Illustration of the moiré polariton system and the constituent moiré excitons and microcavity.** **a**, Schematic of the moiré polariton system formed by excitons confined in moiré lattice and coupled with a planar cavity. **b**, moiré band structure for hBL excitons, where X_1 and X_2 are two bright moiré exciton states. See Method (Theory of moiré excitons) for details of the calculation. **c**, Top panel: theoretical optical absorption spectrum calculated from the moiré exciton band structure. Bottom panel: Reflection contrast spectra near the $MoSe_2$ A exciton resonance, from the WS_2 -$MoSe_2$ hBL (red), $MoSe_2$ ML (blue) and WS_2 ML (green). The spectra are displaced vertically for easier reading. The $MoSe_2$ ML A-exciton (X_A) splits into two well resolved moiré exciton (X_1 and X_2) in the hBN. **d** Angle resolved white light reflection spectrum of the bare cavity, measured in a region where there is no hBL, showing a single cavity dispersion with a half linewidth $\gamma_c = 2.7$ meV.

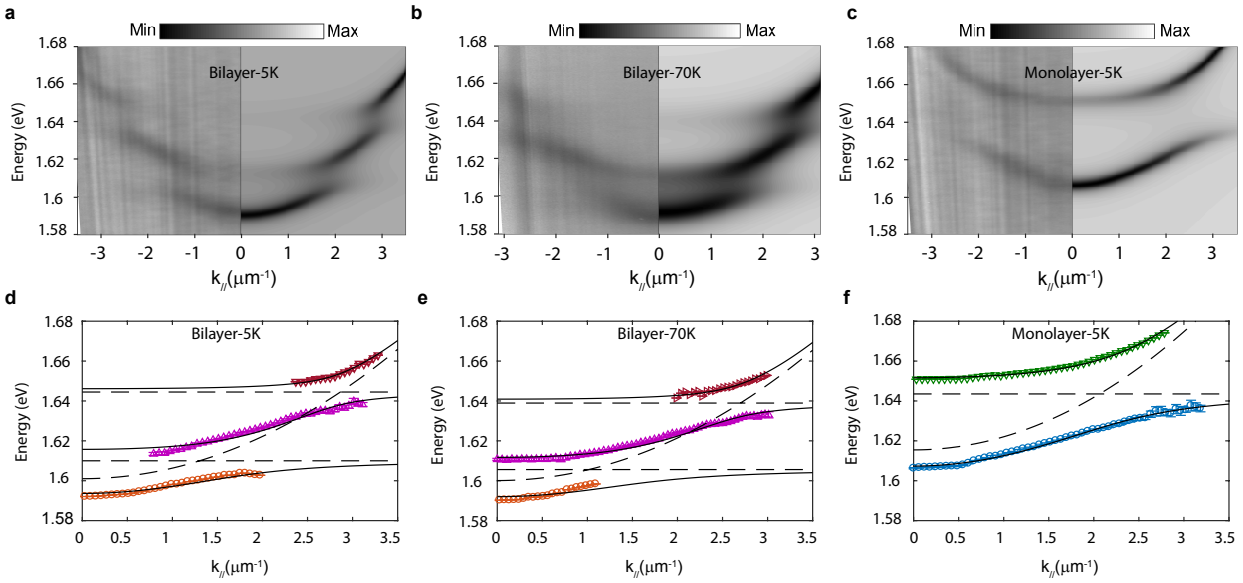

FIG. 2: **Strong coupling and dispersions of moiré and ML polaritonss. a − c**, Angle resolved white light reflection spectra, demonstrating strong coupling between moiré exciton and cavity photon at 5K in **a** and 70K in **b**, in comparison with strong coupling between ML exciton and cavity photon at 5K in **c**. The left/right panels show the measured/simulated results, respectively. **d − f**, The polariton energies vs. in-plane wavenumber $k_{//}$ obtained from **a − c**, respectively. The solid lines are fits to the polariton dispersions with the coupled harmonic oscillator model. The dashed lines are the fitted energies of the uncoupled cavity photon and excitons. The error bars on the energy data correspond to the 95% confidence interval of the Lorentzian fit.

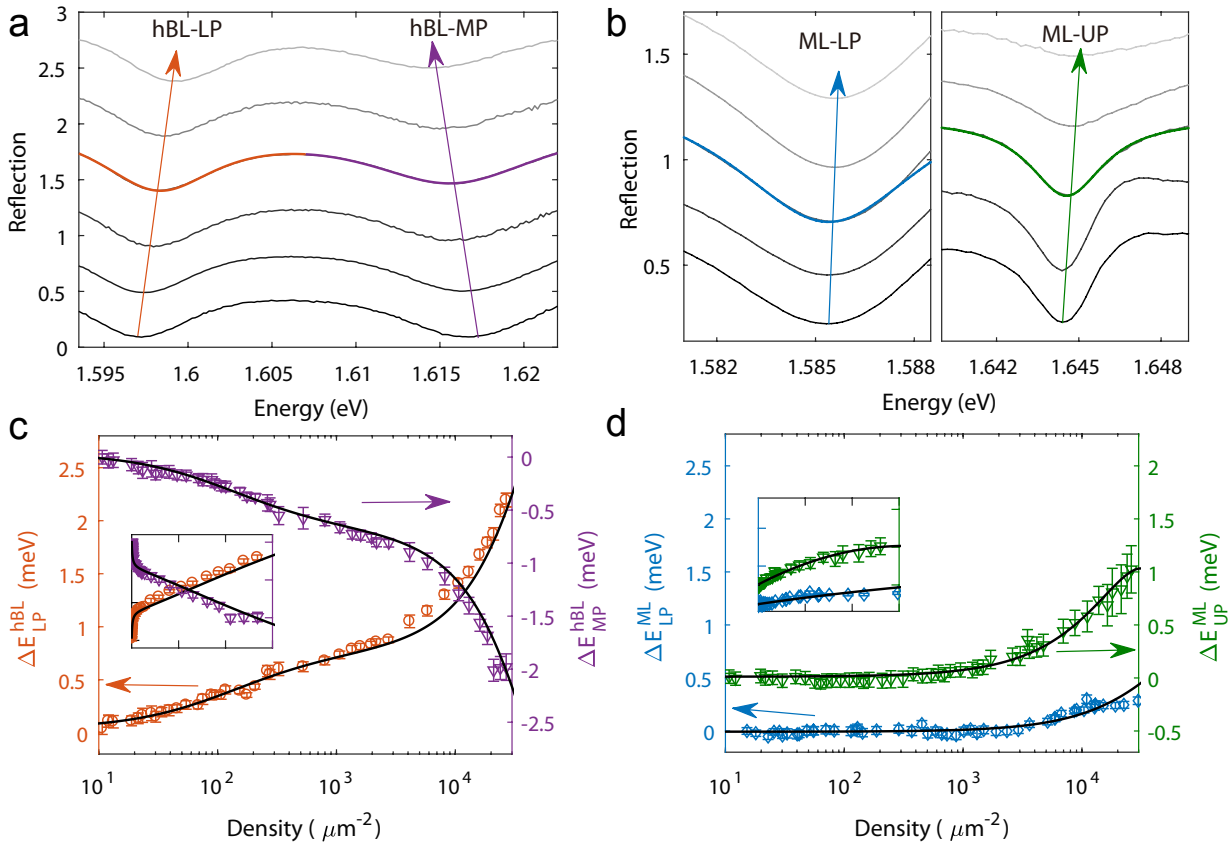

FIG. 3: **Nonlinearity of the moiré hBL and ML polaritons.** **a**, Reflection spectra of moiré LP and MP at zero detuning for different pumping densities. From bottom to top, the carrier density increases from 17 μm^{-2} to 1.8×10^4 μm^{-2}. **b**, Reflection spectra of $MoSe_2$ ML LP (left) and UP (right). The cavity is red detuned from the exciton by 42.5 meV. From bottom to top, the carrier density increases from 22 μm^{-2} to 1.5×10^4 μm^{-2}. In **a**, **b**, the colored solid lines are examples of Lorentzian fits. The arrows are guides for the eyes. **c**, **d** Shift of polariton energies vs. the carrier density (log scale) obtained from **a** and **b**, respectively. Insets show the density in the linear scale, plotted over the same ranges of the horizontal and vertical axes as the main figure. Solid lines are calculations using parameters obtained from fitting the data in Fig. 4 **a** − **c**. The error bars on the energy data correspond to the 95% confidence interval of the Lorentzian fit.

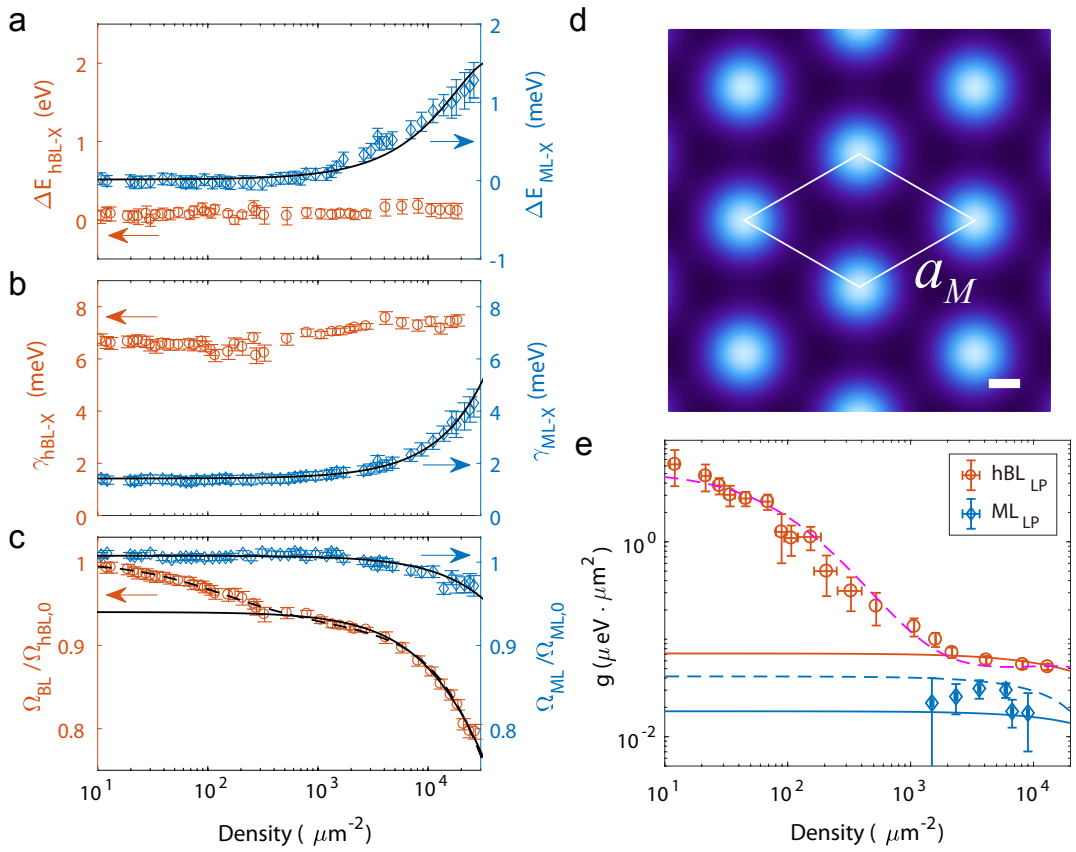

FIG. 4: **Enhanced nonlinearity by moiré lattice confinement.** **a** – **c**, Shift of exciton energy ΔE, half-linewidth γ, and normalized coupling strength Ω/Ω_0 of the hBL-LP (red) and ML-LP (blue) as a function of carrier density, obtained from the data in Fig. 3. The hBL ΔE_{hBL-X} and γ_{hBL-X} (red circles in **a** and **b**) are approximately constant. The ML ΔE_{ML-X} and γ_{ML-X} (blue diamonds in **a** and **b**) are fitted by a second order polynomial and a linear line, respectively (black solid lines in **a** and **b**). In **c**, the black solid lines are fits with equation (3) with a constant n_s for the moiré excitons at n>1000 μm^{-2} and for ML excitons. The black dashed line is a fit with a density-dependent effective saturation density $n_{eff,s}$, and is used for calculating the polariton energies in Fig. 3 **c**. **d**, Real-space distribution of the interlayer component of the X_1 state. The white lines mark a moiré unit cell. The scale bar is 1 nm. **e**, The measured (symbols) and fitted (lines) nonlinear coefficient g vs. carrier density for the moiré hBL-LP (red) and ML-LP (blue). The magenta dashed line and blue solid line are the calculations using the fitted polariton energies in Fig. 3 **c** and **d**. The hBL-LP is at zero detuing; the red solid line and magenta dashed lines correspond to fitted Ω_{hBL} using a constant and effective saturation density, n_s and $n_{eff,s}$, in Eq (3), respectively. For ML-LP, the blue solid and dashed lines correspond to the measured detuning and zero detuning, respectively. The error bars in **a**-**c** and density in **e** are explained in Methods. The error bars of g correspond to the 95%

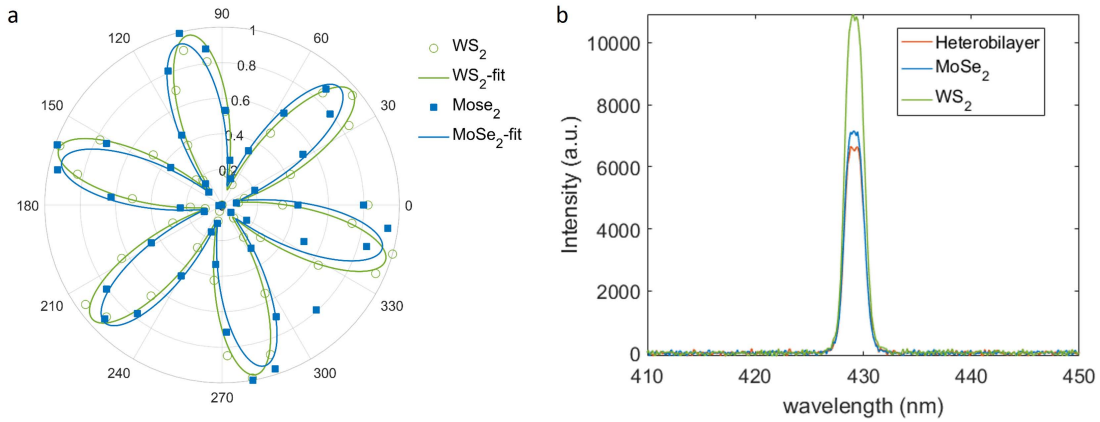

Extended Data Fig. 1: **Heterobilayer twist angle.** Twist angle of hBL in the main text measured by second harmonic generation (SHG) spectroscopy. **a** The polarization-dependent SHG signal measured on the ML WS_2 (green open circles) and MoSe2 (blue filling squares) regions of the hBL, and the corresponding fits with the sinusoidal functions (green and blue solid lines). **b**, the SHG signal from ML WS2 , ML MoSe2 , and hBL regions, measured with the same experimental configurations. The suppressed SHG signal from hBL as a result of destructive interference indicates the stacking order is H-stacking. The twist angle is determined to be $56.5° \pm 0.8°$

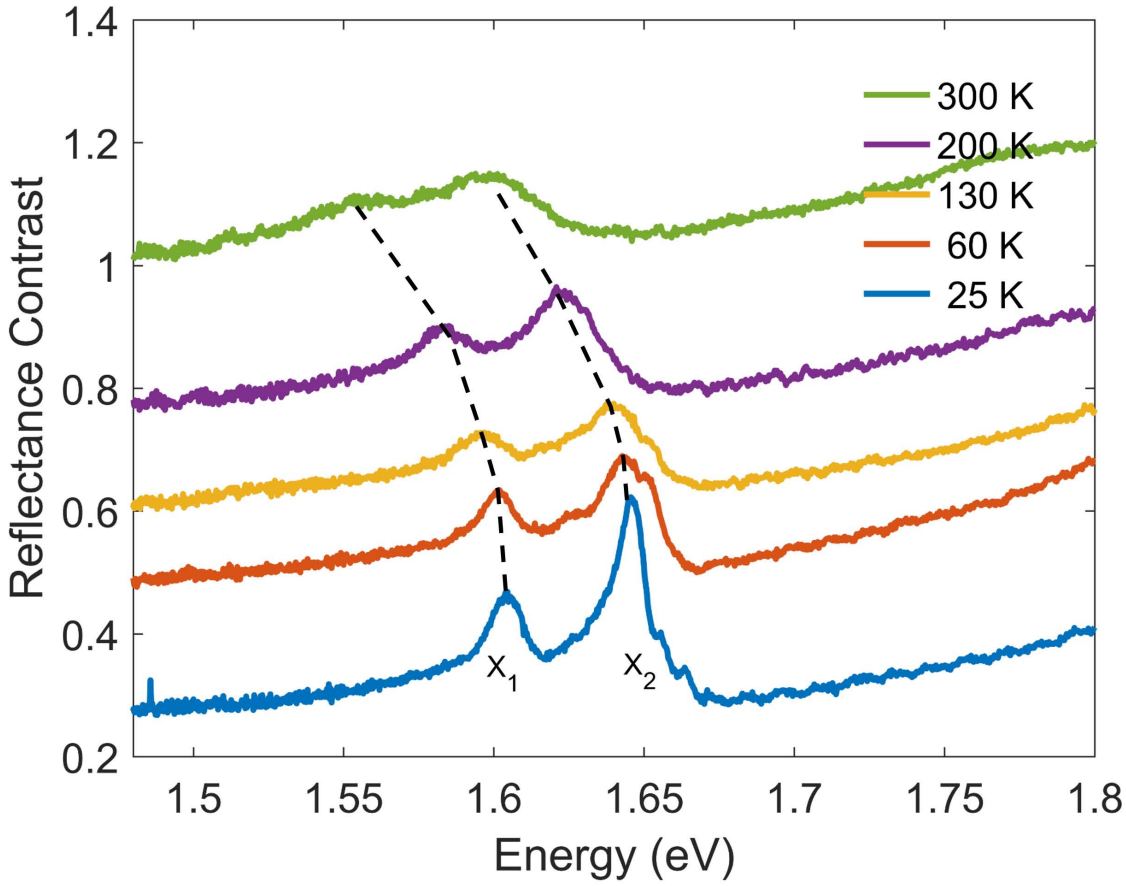

Extended Data Fig. 2: **Temperature dependence of moiré exciton.** Temperature dependence of the moiré exciton X_1 and X_2 measured from a separate heterobilayer prepared on sapphire substrate. The black dashed lines are guides for eyes. The two exciton states can be well resolved up to 200K, which can exclude the possibility of charged exciton or trapped exciton by defect.

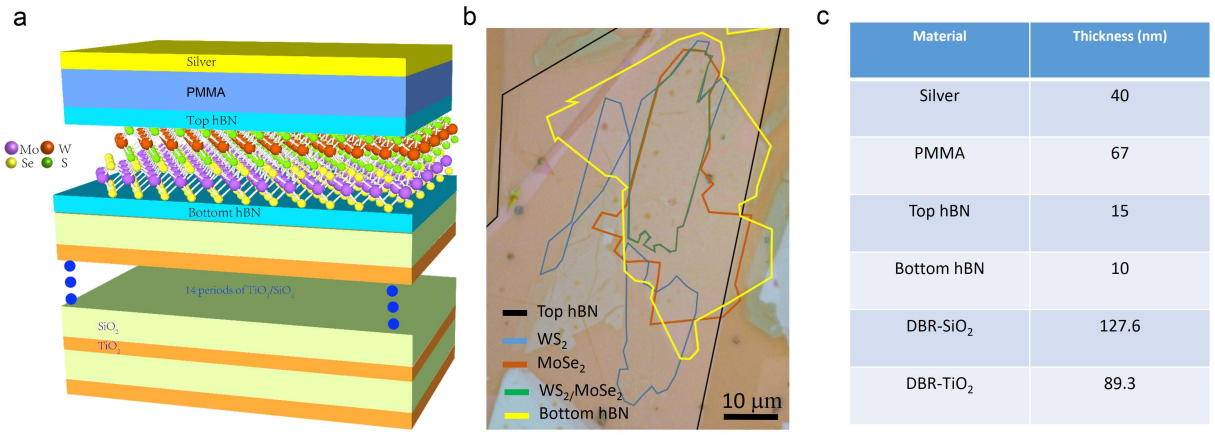

Material	Thickness (nm)
Silver	40
PMMA	67
Top hBN	15
Bottom hBN	10
DBR-SiO_2	127.6
DBR-TiO_2	89.3

Extended Data Fig. 3: **Schematic of the device. a** Schematic of the device shows the different layers of the heterostructure embedded inside a microcavity that consists of a bottom DBR and a top silver mirror. **b** Microscope image of the hBL on the top of DBR mirror, taken before depositing the PMMA layer and the silver mirror. **c** Thickness of each layer for the device.

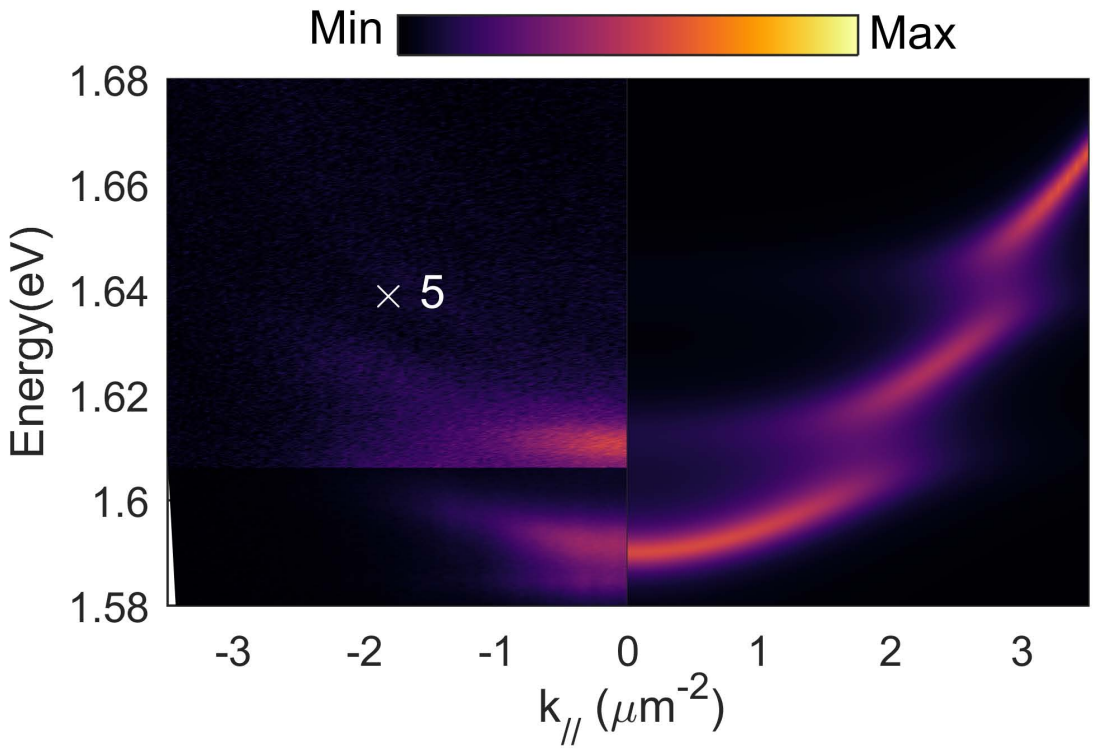

Extended Data Fig. 4: **Photoluminescence from the moiré polariton.** Left panel: Angle resolved photoluminescence spectrum of hBL in cavity, excited by a continuous wave laser at the energy of 2.3 eV and power of 50 μW. To enhance the visibility of states at higher energy, emission intensity above 1.607 eV is magnified by 5 times. Right panel: simulated angle resolved absorption, which agrees well with the measurement.

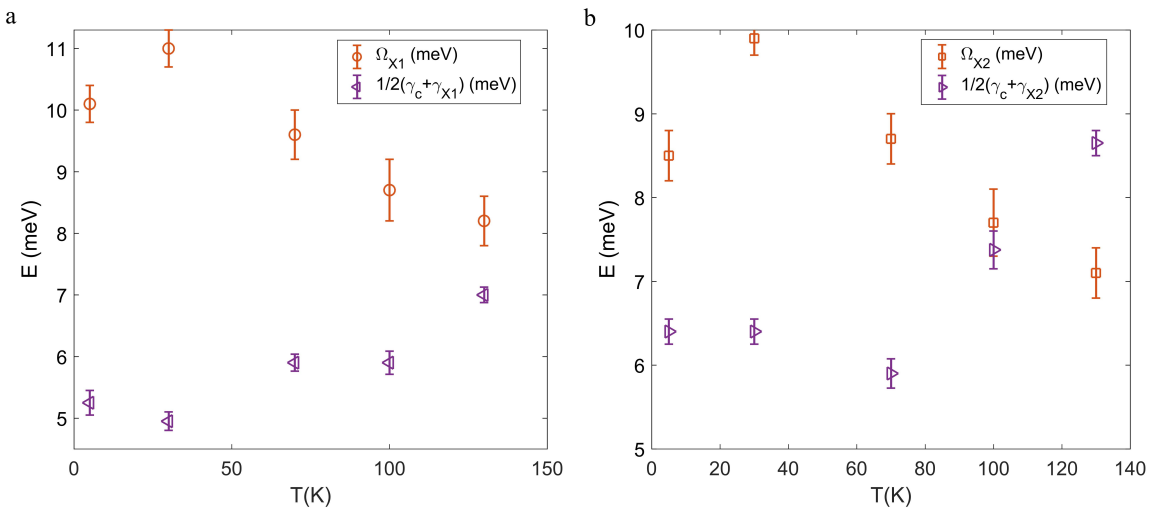

Extended Data Fig. 5: **Transition from strong coupling to weak coupling driven by thermal broadening.** Strong coupling to weak-coupling transition measured by temperature dependence of Ω_1 (red open circles), $(\gamma_c + \gamma_{X1})/2$ (purple left-triangle) in **a** and Ω_2 (red square), $(\gamma_c + \gamma_{X2})/2$ (purple right-triangle) in **b**. $\gamma_c = 2.7meV$ is constant with temperature. γ_{X1} and γ_{X2} are measured independently from bare hBL. Ω_1 and Ω_2 drop below the average linewidth at about 100K, showing the transition to the weak-coupling regime.

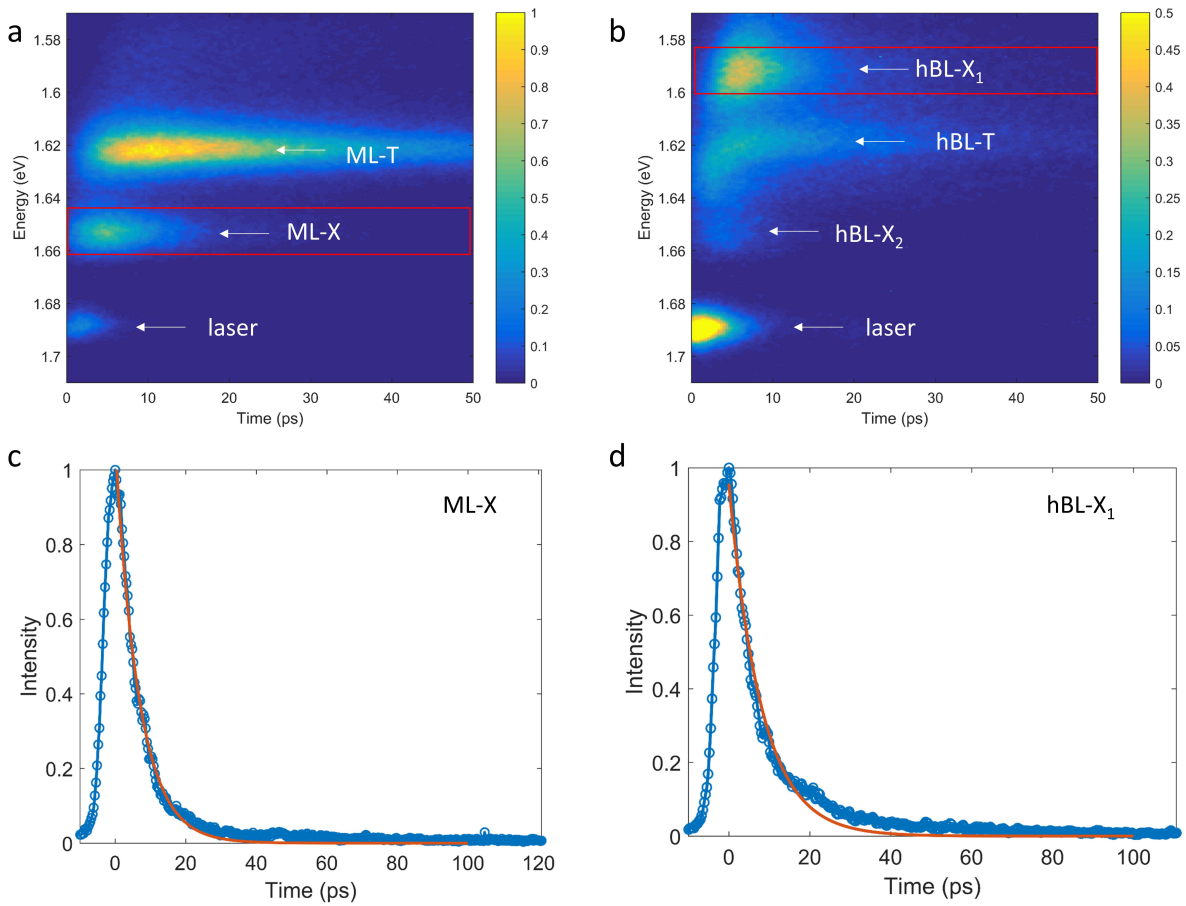

Extended Data Fig. 6: **Time resolved photoluminescence (TRPL) of ML exciton, ML trion, hBL excitons, and hBL trion.** TRPL spectra measured by streak camera for ML $MoSe_2$ (ML) **a** and hBL WS_2 /$MoSe_2$ (hBL) **b**. (The hBL data is collected from a different sample from the main text, which is not integrated with microcavity) The different resonances are labelled with white arrows including ML exciton (ML-X), ML trion (ML-T), moiré exciton at higher energy (hBL-X_2), moiré excion at lower energy (hBL-X_1), and moiré trion (hBL-T). **c** and **d** shows the time resolved decay of ML-X and hBL-X_1 respectively by integrating the spectrum in the range labeled by the red rectangles in a and b. The red solid lines in **c** and **d** are the fits with single exponential decay function. PL decay time for ML-X and hBL-X_1 are 6.7 ps and 8.0 ps respectively.

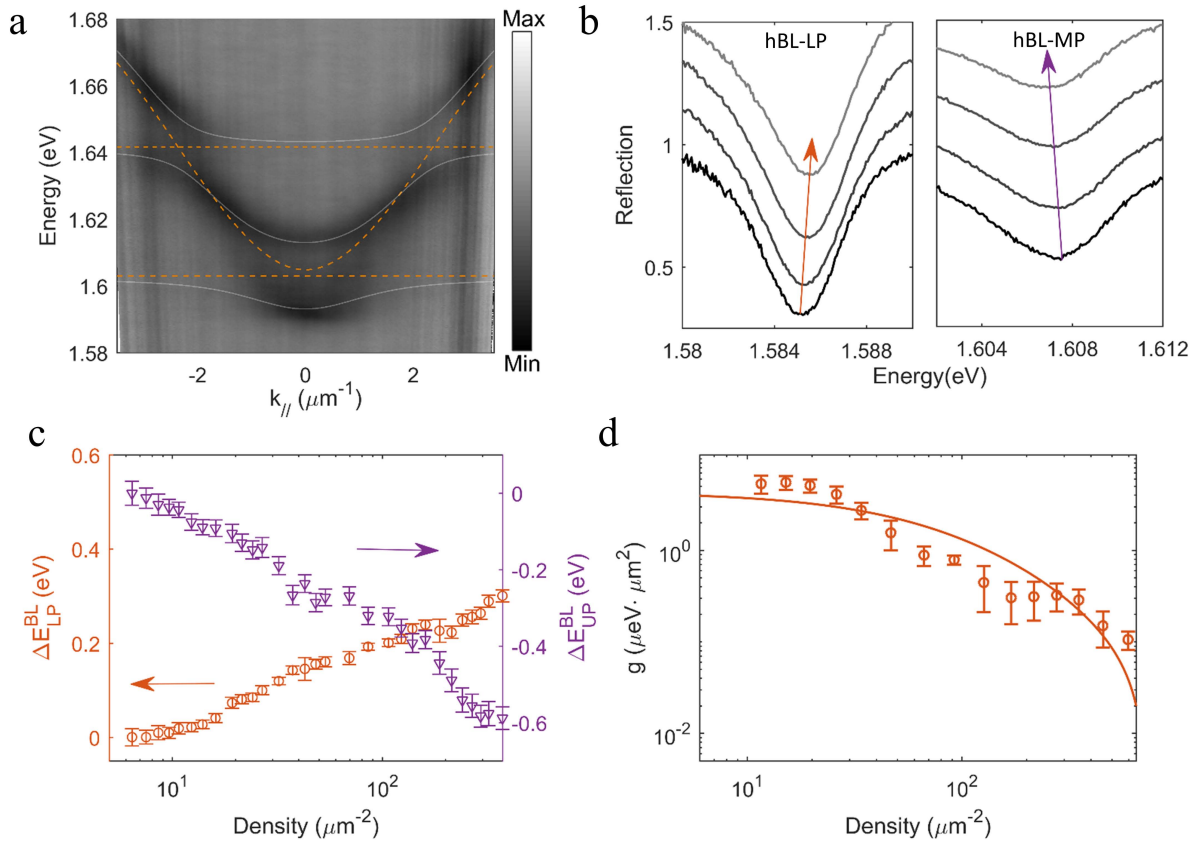

Extended Data Fig. 7: **Strong nonlinearity measured in another device.** Measurement taken on a different sample shows reproducibility of the results. **a** Angle resolved white light reflection spectra taken at 5K on the second sample. White solid lines are the fits using coupled oscillator model. The dashed white lines are the fitted energies of the uncoupled cavity photon and excitons. **b** Power dependent reflection spectra for the lower polariton (left panel) and middle polariton (right panel).**c** Shift of polariton energies vs. the carrier density (log scale) obtained from **b**. **d** Extracted nonlinear coefficients for lower polariton (red circles) and the calculations using fitted polariton energies (solid line).

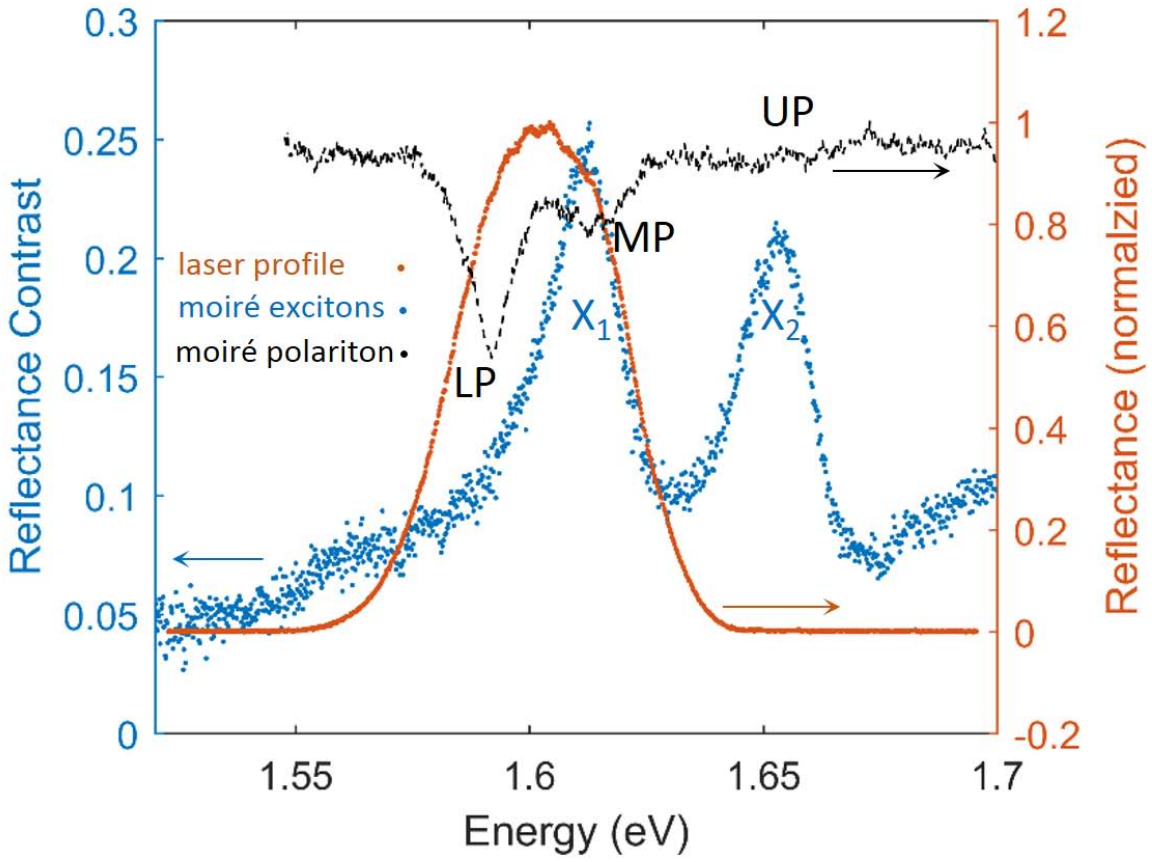

Extended Data Fig. 8: **Profile of the laser used for nonlinearity characterization.** Profile of pulsed laser (red dot) used for the nonlinearity measurement of moiré polaritons, compared with the moiré exciton X_1 and X_2 (blue dots), and moiré polaritons (black dots). The laser has a negligibly small tail on X_2 and upper polariton.

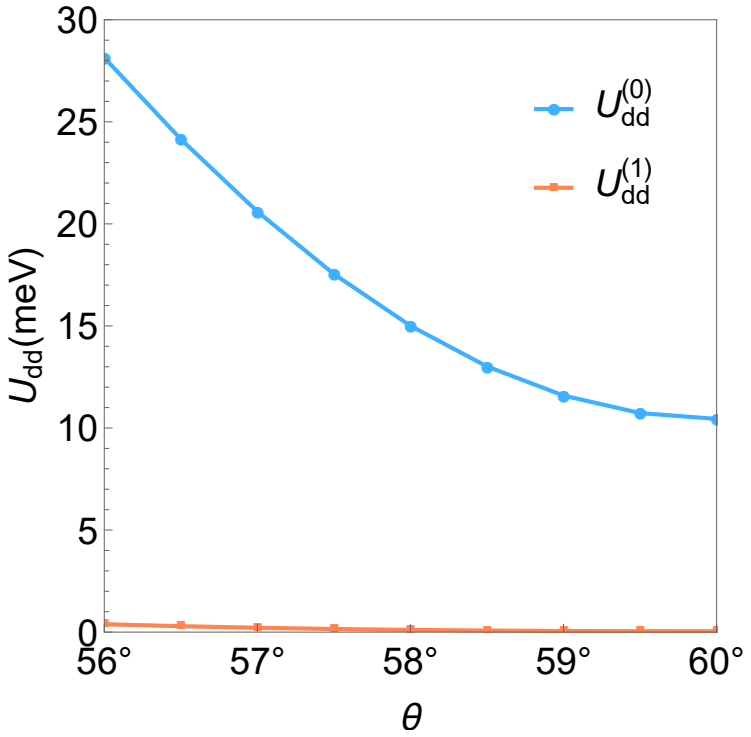

Extended Data Fig. 9: **Dipole-Dipole interaction strength as a function of twist angle θ.**

$U_{dd}^{(0)}$ and $U_{dd}^{(1)}$ are respectively onsite and nearest-neighbor interaction strength.

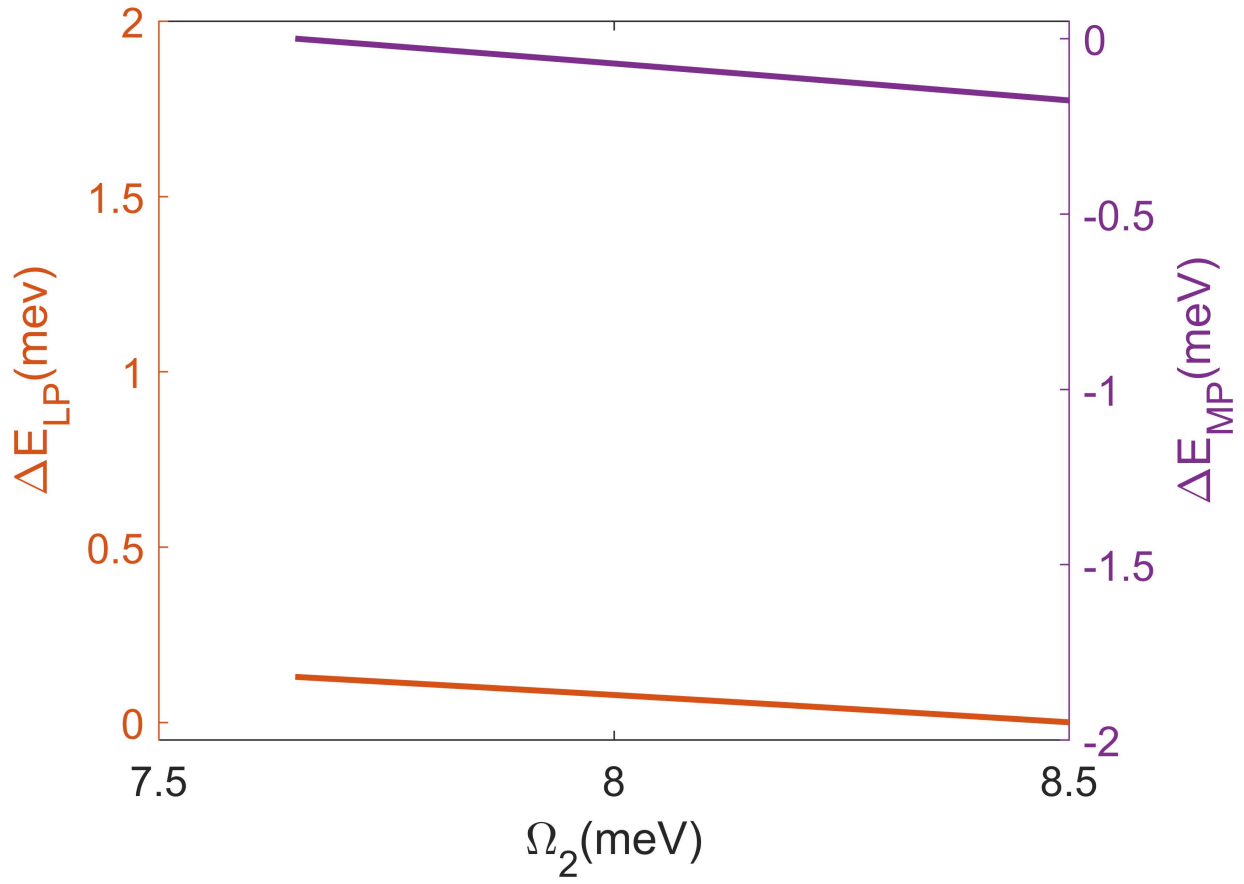

Extended Data Fig. 10: **Effect on the nonlinearity from the moiré exciton X_2.** Energy shifts of E_{LP}^{BL} and E_{MP}^{BL} from the saturation of upper moiré exciton X_2. In the main test, we ignore the effects of moiré exciton X_2 on the nonlinearity of lower and middle polaritons. To quantitatively estimate the effects, we calculate the ΔE_{LP}^{BL} and ΔE_{MP}^{BL} as a function of coupling strength (Ω_2) of X_2. When the Ω_2 changes by 10%, the E_{LP} and E_{MP} will shift within 0.16 meV, which is less than 8% of the shift observed from the experiments (2meV) (Fig. 3c in the main text). So the change of E_{LP} and E_{MP} induced by Ω_2 can be safely ignored for simplicity.